



# PHOTONICS Research

## Micro-transfer printing of O-band InAs/GaAs quantum-dot SOAs on silicon photonic integrated circuits

YANG LIU,<sup>1,†,\*</sup> JING ZHANG,<sup>1,†</sup> LAURENS BOGAERT,<sup>1</sup> EMADREZA SOLTANIAN,<sup>1</sup> EVANGELIA DELLI,<sup>1</sup> KONSTANTIN MOROZOV,<sup>2</sup> SERGEY MIKHRIN,<sup>2</sup> JOHANNA RIMBÖCK,<sup>3</sup> GUY LEPAGE,<sup>4</sup> PETER VERHEYEN,<sup>4</sup> JORIS VAN CAMPENHOUT,<sup>4</sup> PETER OSSIEUR,<sup>5</sup> GEERT MORTHER,<sup>1</sup> AND GUNTHER ROELKENS<sup>1</sup>

<sup>1</sup>Photonics Research Group, INTEC, Ghent University - imec, 9052 Ghent, Belgium

<sup>2</sup>Innolume GmbH, 44263 Dortmund, Germany

<sup>3</sup>EV Group E.Thallner GmbH, 4782 St. Florian am Inn, Austria

<sup>4</sup>IMEC, 3001 Heverlee, Belgium

<sup>5</sup>IDLab, INTEC, Ghent University - imec, 9052 Ghent, Belgium

<sup>†</sup>These authors contributed equally to this work.

\*Corresponding author: yangyliu.liu@ugent.be

Received 25 October 2024; revised 21 January 2025; accepted 7 March 2025; posted 10 March 2025 (Doc. ID 545946); published 30 April 2025

Silicon photonics (SiPh) technology has become a key platform for developing photonic integrated circuits due to its CMOS compatibility and scalable manufacturing. However, integrating efficient on-chip optical sources and in-line amplifiers remains challenging due to silicon's indirect bandgap. In this study, we developed prefabricated standardized InAs/GaAs quantum-dot (QD) active devices optimized for micro-transfer printing and successfully integrated them on SiPh integrated circuits. By transfer-printing standardized QD devices onto specific regions of the SiPh chip, we realized O-band semiconductor optical amplifiers (SOAs), distributed feedback (DFB) lasers, and widely tunable lasers (TLs). The SOAs reached an on-chip gain of 7.5 dB at 1299 nm and maintained stable performance across a wide input power range. The integrated DFB lasers achieved waveguide (WG)-coupled output powers of up to 19.7 mW, with a side-mode suppression ratio (SMSR) of 33.3 dB, and demonstrated notable robustness against optical feedback, supporting error-free data rates of 30 Gbps without additional isolators. Meanwhile, the TLs demonstrated a wavelength tuning range exceeding 35 nm, and a WG-coupled output power greater than 3 mW. The micro-transfer printing approach effectively decouples the fabrication of non-native devices from the SiPh process, allowing back-end integration of the III-V devices. Our approach offers a viable path toward fully integrated III-V/SiPh platforms capable of supporting high-speed, high-capacity communication. © 2025 Chinese Laser Press

<https://doi.org/10.1364/PRJ.545946>

### 1. INTRODUCTION

Silicon photonics has emerged as a leading technology for creating compact, cost-effective, and highly scalable photonic circuits, benefiting from advancements in CMOS technology [1–3]. The SiPh platform has reached a mature stage, enabling the realization of low-loss, high-density Si and SiN waveguides, WDM filters, as well as low-loss edge couplers and grating couplers, which effectively link on-chip waveguides and off-chip fibers [4,5]. In terms of active components, mature platforms now can support over-56-Gbps silicon ring modulators, Mach-Zehnder modulators, and GeSi electro-absorption modulators [6]. Meanwhile, high-speed Ge photodetectors on silicon are available for OE signal conversion [7–9]. This integration of a wide range of active and passive photonic

components on a silicon wafer using a mature tool set facilitates high-speed optical transceivers, further enhancing the potential of silicon photonics in advanced communication systems [10–12].

Despite the advanced capabilities of the SiPh platform, several critical building blocks remain missing for achieving fully integrated and compact photonic systems-on-chip. One of the most crucial components for silicon photonics is a laser [13–16]. A primary limitation is that silicon is an indirect bandgap semiconductor [17]. Efficient light emission cannot be achieved, which is a critical requirement for photonic systems. Additionally, an in-line optical amplifier on-chip is essential because each photonic building block introduces insertion loss, leading to significant signal attenuation after the

optical signal has traversed multiple components on the chip. In traditional fiber optic communications, erbium-doped fiber amplifiers (EDFAs) for the C-band and praseodymium-doped fiber amplifiers (PDFAs) for the O-band are commonly used to mitigate such losses [18,19]. However, miniaturizing these amplifiers for on-chip integration remains a challenge and still requires a pump laser source. Furthermore, it is essential to prevent reflections that arise as light passes through optical components, as lasers are typically sensitive to external feedback. Therefore, on-chip optical isolators and circulators are required [20–22]. However silicon lacks magneto-optic effects [23], precluding the fabrication of effective optical isolators or circulators on-chip.

Several useful semiconductor, electro-optic and magneto-optic materials have shown promise in addressing these limitations of silicon photonics. Notably, III–V semiconductors such as InP, GaAs, and GaN are highly effective for the realization of light sources across a wide spectral range, from near-ultraviolet to infrared [24–28]. Additionally, materials like lithium niobate (LN), lithium tantalate ( $\text{LiTaO}_3$ ), and lead zirconate titanate (PZT), due to their non-centrosymmetric crystal structures, are well-suited for high-performance electro-optic modulators [29–32]. Furthermore, magneto-optical materials such as cerium-substituted yttrium iron garnet (Ce:YIG) are ideal for optical isolators [33–35]. However, the integration of these materials into SiPh platforms presents significant challenges due to their non-CMOS compatibility.

Overcoming these limitations is crucial for the advancement of fully integrated photonic systems. Micro-transfer printing ( $\mu\text{TP}$ ), a technology available under license from X-Celeprint, Ltd., offers a promising solution by decoupling the fabrication of non-native devices from the SiPh platform, enabling versatile integration across various material systems and substrates [36–39]. This technique provides several key advantages, including high alignment accuracy within 500 nm, high throughput, and the capability for dense integration with thousands of devices per reticle, making it a cost-effective solution for moderately high-volume production. Other mainstream approaches for heterogeneous integration, such as wafer bonding, flip-chip integration, and hetero-epitaxial growth, also have their merits.

A detailed comparison of these techniques is available in Ref. [36].

In this study, we pre-fabricated high-density standardized InAs/GaAs quantum dot (QD) active devices on GaAs epitaxial wafers, optimized for micro-transfer printing. The QD layers exhibit lower reflection sensitivity compared to multiple quantum well (MQW) structures, potentially avoiding the need for additional optical isolators. The QD devices can be easily released and transfer-printed onto the target regions of the SiPh chip. These QD devices were subsequently used to form DFB lasers, widely tunable lasers, and SOAs on-chip, providing light sources and amplifiers for silicon photonics, demonstrating the potential for advanced device integration.

## 2. DESIGN AND FABRICATION

### A. Pre-fabrication of GaAs QD Active Devices

To prevent contamination of the SiPh process line with non-CMOS-compatible materials, we pre-fabricated standardized InAs/GaAs QD active devices on GaAs epitaxial wafers. The overall process flow for integrating these GaAs QD devices onto an advanced SiPh platform, such as the imec iSiPP50G [6] platform, is illustrated in Fig. 1.

The fabrication process begins with the definition of the GaAs mesa on the epitaxial wafers [Figs. 1(a) and 1(b)] using inductively coupled plasma (ICP) etching, followed by metal deposition. Afterwards, the mesa is encapsulated with a thick double-dielectric layer of  $\text{SiN}_x$  and  $\text{SiO}_2$ , and the surface topography is planarized with a thick benzocyclobutene (BCB) layer. Details of the fabrication process can be found in our previous work [40]. To release the GaAs QD active devices, the sample undergoes a release etching process by immersing it in a 1:1 solution of 37% hydrochloric acid (HCl) and water for 1 h. This wet etching step selectively removes the AlGaAs sacrificial layer, leaving the QD devices intact and suspended above the substrate while still supported by photoresist tethers. At this stage, the QD active device array is fully fabricated and ready for transfer. Figure 2(a) shows optical microscope images of the fabricated QD device array on the source wafer, after the selective wet etching, ready for pick-up using a polydimethylsiloxane (PDMS) stamp.

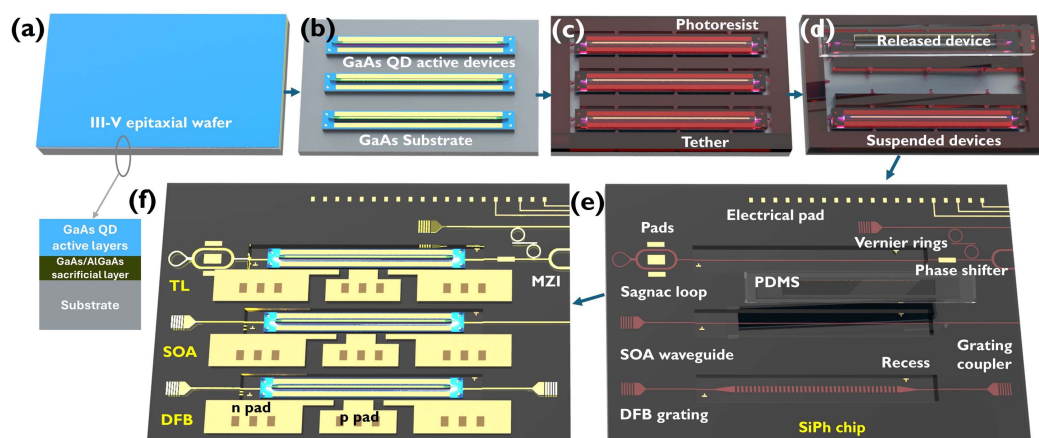


**Fig. 1.** Schematic process flow for the integration of GaAs QD active devices on a SiPh platform.

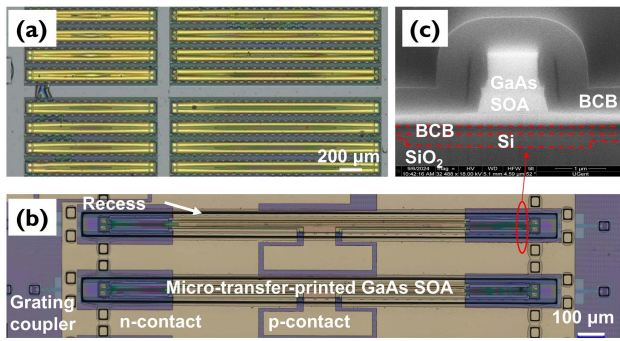


**Fig. 2.** (a) Optical microscope images of the fabricated GaAs QD device array on the source wafer; (b) micro-transfer printed GaAs QD-on-Si SOAs on the SiPh chip; (c) cross-sectional SEM image of the taper region.

The photoresist tethers, fabricated through photolithography [Fig. 1(c)], play a critical role in securing the QD devices during the releasing process. These tethers provide better compliance and effectively minimize mechanical stress. The pitch of the tethers is designed to provide adequate support for the III–V coupon, preventing collapse while ensuring easy detachment at the anchor points during the pick-up process. However, excessive density or overly long tethers may leave residual tether fragments on the coupon after breaking, potentially leading to bonding failure. The origin and development of the  $\mu$ TP process for various materials and devices are comprehensively detailed in our previously published reference papers [41–43].

## B. Integration of GaAs QD-on-Si Amplifiers

We utilized the IMEC SiPh platform to fabricate SiPh circuits, which can integrate low-loss waveguides, grating couplers (GCs), electrical interconnects, and more. The silicon waveguide circuits were realized on imec’s 300 mm SiPh platform, which consists of a 220 nm crystalline silicon device layer with a 160 nm thick poly-Si overlay layer and a complex back-end layer stack including two metal interconnect layers and exposed Al bond pads. The 2  $\mu$ m thick buried oxide (BOX) layer beneath the silicon waveguide serves as the insulating layer, ensuring proper confinement of the optical mode within the silicon waveguide, minimizing losses. Recesses were defined on the platform to accommodate the GaAs QD devices after

transfer printing, as shown in Fig. 1(e). To address excessive roughness, which could compromise bonding quality, the surface was smoothed by filling with a thin BCB layer (tens of nanometers thick), maintaining sufficient adhesion for the subsequent placement of the GaAs active devices. Using an X-Celeprint MTP100 lab-scale printer, the QD devices were picked up with PDMS stamps of the corresponding size, as shown in Fig. 1(d). The devices are then precisely transfer-printed into the designated recesses, achieving a positional alignment error of less than 500 nm. After the coupons are transferred, the BCB is fully cured at 280°C, ensuring a robust and durable bond. Following this, standardized metallization processes are employed to form the electrode pad, effectively connecting the GaAs QD devices to the on-chip electrodes of the SiPh chip. Figure 2(b) shows the optical microscope image of QD devices positioned within the recesses of the SiPh wafer after the final metallization.

Figures 3(a) and 3(b) illustrate the schematic of the GaAs QD semiconductor optical amplifier (SOA) devices integrated onto the SiPh waveguide circuit. The optical signal is efficiently coupled from the crystalline silicon (c-Si) waveguide to the polycrystalline (p-Si)/crystalline silicon waveguide, and then finally coupled into the GaAs QD active layers via an adiabatic taper [40], which is designed to provide a 1  $\mu$ m alignment tolerance. Figures 3(d) and 3(e) present the simulated coupling efficiency ( $|S_{21}|^2$ ) of the taper as functions of misalignment, demonstrating a transmission efficiency of 99.1% at 1  $\mu$ m misalignment. The feedback levels are below –40 dB at the taper tip interface. The cross-sectional SEM image of the taper tip is shown in Fig. 2(c).

## C. Integration of GaAs QD-on-Si DFB Lasers

For the integration of GaAs QD lasers on the SiPh platform, the SiPh target chip for the laser was fabricated at imec using 193 nm immersion deep ultraviolet (DUV) lithography. The passive SiPh chip consists of a c-Si layer and a p-Si layer on a 2  $\mu$ m BOX layer. The c-Si layer was etched to define the waveguide structures and the second-order Bragg grating (grating period of 390 nm, grating length of 1.4 mm, full etch through the c-Si) with a quarter-wavelength ( $\lambda/4$ ) phase shift [40,44,45].

After back-end fabrication and cavity definition, a thin BCB layer, on the order of tens of nanometers, was applied on the

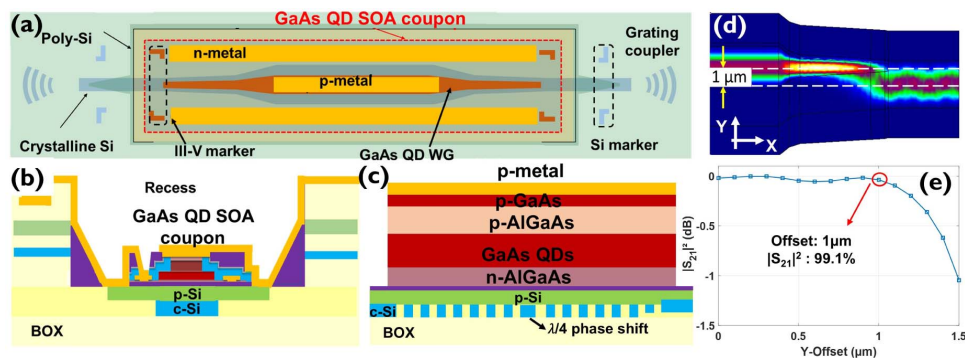


**Fig. 3.** (a) Top-view schematic of the GaAs QD devices after transfer printing onto the SiPh platform; (b) cross-sectional schematic of the GaAs QD-on-Si devices along the  $y$ -direction; (c) cross-sectional schematic of the QD devices on Bragg grating along the  $x$ -direction; (d) optical mode field distribution during coupling through the taper structure; (e) coupling efficiency ( $|S_{21}|^2$ ) of the taper as a function of misalignment.

top of the p-Si layer to facilitate the transfer and adhesion of the QD devices, similar as for the SOAs. After transfer-printing, the QD devices function as the gain medium for the DFB lasers on SiPh. The DFB grating in the c-Si layer selectively reflects light at the Bragg wavelength and enforces single-mode operation by allowing only the desired wavelength to resonate. Figure 3(c) shows the cross-sectional schematic of the QD devices on the Bragg grating. This process leads to the emission of a coherent laser beam with a well-defined wavelength and a high spectral purity, characteristic of DFB lasers on SiPh.

#### D. Integration of GaAs QD-on-Si Widely Tunable Lasers

To integrate GaAs QD widely tunable lasers onto the SiPh platform, Fig. 4(a) shows a schematic layout of the SiPh circuit, illustrating the key components. The chip includes a gain region for integrating a GaAs QD SOA, a Vernier filter, a tunable Sagnac loop mirror, a phase shifter, and a Mach-Zehnder interferometer (MZI)-based switch.

The Vernier filter consists of two thermally tunable micro-ring resonators (MRRs) with slightly different diameters (60 and 63  $\mu\text{m}$ ), corresponding to free spectral ranges (FSRs) of 2.34 and 2.23 nm, respectively, around 1310 nm wavelength. This configuration enables the filter to select wavelengths over a broader tuning range than each individual resonator [46–48]. The thermo-optic phase shifter is used to tune the cavity modes of the laser. A thermally tunable reflector is implemented as an out-coupling mirror, enabling control of the mirror's reflectivity for optimal out-coupling efficiency. As shown in Fig. 4(a), an additional region was reserved on the chip for integrating GaAs QD devices to amplify the light output from the tunable reflector (although QD coupons were not printed in this region of the current chip). The MZI-based switch is used to direct the output power either to the test port (grating coupler) or to other on-chip components for further manipulation.

Following the transfer-printing of 2.2 mm long GaAs QD active devices onto the gain region of the chip, the subsequent processing steps were identical to those used in fabricating our GaAs QD DFB lasers. The longer SOA coupon was selected to enhance optical gain and reduce electrical resistance. This design also mitigates self-heating. Figure 4(b) shows a microscope image of the fully fabricated tunable laser on the SiPh chip.

### 3. CHARACTERIZATION AND DISCUSSION

#### A. Performance of Integrated GaAs QD-on-Si Amplifiers

The O-band GaAs QD-on-Si SOAs were placed on a temperature-controlled stage for all measurements. The devices under test were optically probed using cleaved standard single-mode fibers on a fiber stage. The GaAs QD SOAs were electrically contacted using probe needles. A Keithley 2400 SourceMeter was used to drive the active devices and obtain their *IV* characteristics. From Fig. 5(a), the SOAs have a differential resistance ranging from 3.89  $\Omega$  to 3.73  $\Omega$ , for a surface area of 5520  $\mu\text{m}^2$ , when the temperature of the stage changed from 20°C to 50°C. The differential resistance was determined for an injection current density of 2.5 kA/cm<sup>2</sup>. The amplifier's good electrical characteristics enable high current injection with minimal self-heating, which is crucial for high-power operation.

To accurately characterize the on-chip gain of the SOAs, a stable continuous-wave (CW) tunable laser (Santec TSL-510) was used, connected to a polarization controller to optimize coupling efficiency into the on-chip grating coupler. The angle of the fiber holders was adjusted to align the wavelength of maximum transmission with the gain peak of the SOAs. The output power of the SOA was measured using an optical spectrum analyzer (OSA, Agilent 86140B) set to a resolution bandwidth (RBW) of 0.1 nm. This narrow bandwidth was critical to ensuring that the measured output power was not affected by amplified spontaneous emission (ASE), thereby

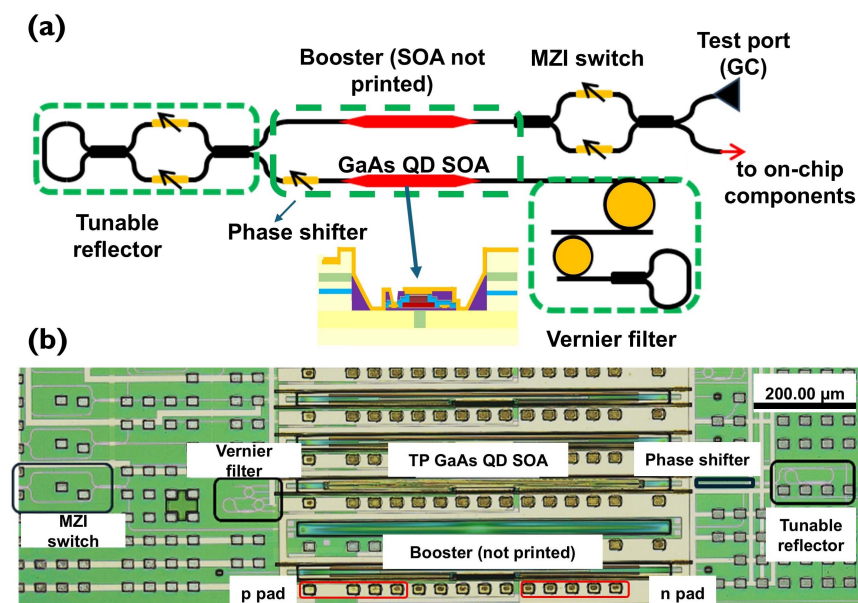
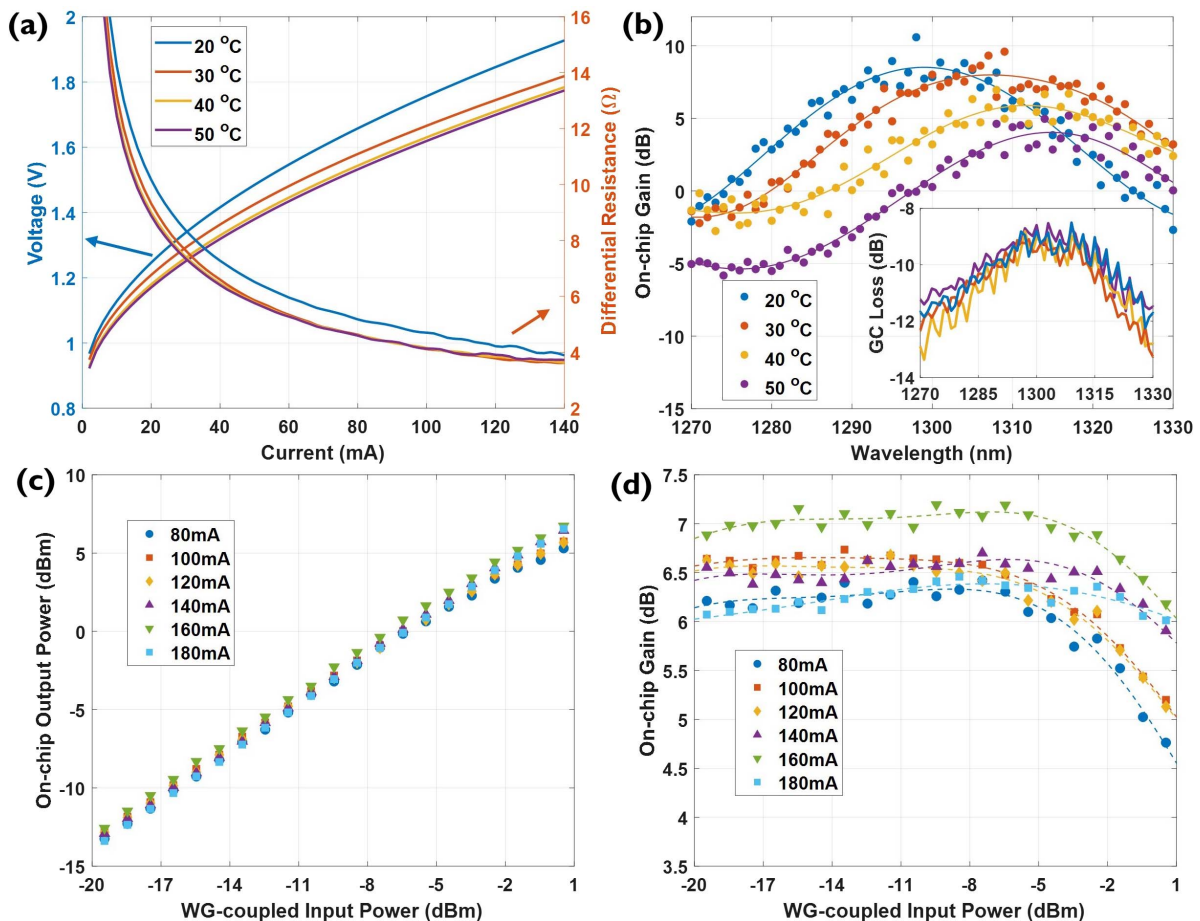


Fig. 4. (a) Schematic of the SiPh circuit for the widely tunable laser; (b) microscope image of the fully fabricated tunable laser on the SiPh chip.



**Fig. 5.** (a) Current-voltage ( $I/V$ ) characteristics and differential resistance of the GaAs QD-on-Si SOA at various temperatures; (b) on-chip gain spectrum of the GaAs QD-on-Si SOA as a function of wavelength at different temperatures, with the inset showing single GC loss versus wavelength and temperature; (c) on-chip output power versus waveguide (WG)-coupled input power at different bias currents; (d) on-chip gain as a function of WG-coupled input power for various bias currents.

providing an accurate evaluation of the amplifier's performance at the specified wavelength.

Additionally, to calibrate the on-chip gain measurements, it was necessary to accurately quantify the grating coupler losses as a function of wavelength [inset of Fig. 5(b)]. To achieve this, short straight reference passive silicon waveguides, each with two grating couplers, were integrated onto the chip, strategically placed near the amplifiers. This placement ensured that the reference waveguides experienced the same fabrication processes as those applied to the passive waveguides and couplers within the SOAs. The losses of the grating couplers were determined using the same measurement setup as for the SOAs, ensuring consistency in the experimental conditions and providing reliable data for calibrating the amplifier gain.

Figure 5(b) illustrates the relationship between the input wavelength and the corresponding gain of the SOA (1.66 mm long) at various temperatures after calibration. It shows that the SOA achieves its maximum gain of 7.51 dB at a wavelength of 1299 nm when the device is maintained at 20°C. As the temperature of the measurement stage increases, there is a decrease in the gain of the SOA from 7.51 to 4.03 dB. Concurrently, the peak gain wavelength exhibits a red shift, moving from 1299 nm at 20°C to 1314 nm at 50°C. The observed redshift

with increasing temperature can be attributed to the temperature dependence of the bandgap energy in the active region material. Specifically, the bandgap of the QD active region decreases approximately linearly with increasing temperature [49–51]. As the bandgap narrows, the energy required for electron transitions decreases, causing the optimal wavelength for gain to shift toward longer wavelengths, hence the observed redshift. Moreover, at elevated temperatures, non-radiative recombination processes, such as Auger recombination and defect-related recombination, become more pronounced [52–54]. These processes lead to a reduction in the number of free carriers available for stimulated emission, thereby reducing the population inversion necessary for optical amplification. Consequently, the gain of the SOA decreases as temperature increases. In future work, further optimization of the device structure will be explored. The inclusion of thermal vias to the substrate will enable realizing a lower thermal impedance, further reducing self-heating, and improving the high temperature performance of the devices.

Figures 5(c) and 5(d) present the on-chip output power and the corresponding gain of the SOA as a function of the input power. This characterization was conducted by varying the input power of a tunable laser set to a wavelength of 1300 nm.

The on-chip input power was adjusted between  $-20$  dBm and  $+1$  dBm while the SOA output power was monitored using an OSA. The SOAs were biased at different currents ranging from 80 to 180 mA. The results indicate a linear relationship between the waveguide-coupled input power and the on-chip output power, particularly when the input power is below  $-5$  dBm. Upon calibrating the gain at different drive currents, it is observed that the gain remains stable for input powers below  $-5$  dBm. To achieve optimal performance, the mode field design in the coupling region must balance the trade-off between saturation output power and gain. This balance directly impacts the efficiency and effectiveness of the SOA design.

## B. Performance of Integrated GaAs QD-on-Si DFB Lasers

The GaAs QD-on-Si DFB laser testing setup is identical to the SOA testing setup, as described above. The optical power was then measured using a power meter (HP 8163A). Figure 6(a) presents the light-current-voltage (*LIV*) curves of the DFB laser at different stage temperatures. As shown, the DFB laser begins to lase when the drive current exceeds 70 mA. With further

increase in drive current, the waveguide-coupled output power gradually rises, reaching a maximum of 19.7 mW at 230 mA at a measurement temperature of 20°C. The WG-coupled output power represents the optical power within the silicon waveguide on chip, calibrated to exclude losses from the fiber-to-grating coupler interface and other system losses.

When the stage temperature is increased to 40°C, the peak optical power shift is obtained at 216 mA with a reduced peak power of 14.1 mW, after which the optical power begins to decline as the drive current continues to increase. This behavior can be attributed to the laser diode's reduced efficiency in converting electrical energy into optical energy at elevated temperatures. Additionally, as the drive current surpasses a certain threshold, the additional heat generated exacerbates these effects, leading to a decrease in output power. This explains the earlier peak and subsequent roll-off observed in the *LI* curve at 40°C. The kinks in the *LI*-curve are attributed to reflection from the grating couplers used to characterize these devices.

Figure 6(b) shows the optical spectrum of the output power at 20°C. At lower drive currents, the DFB laser exhibits mode competition. However, as the drive current increases,

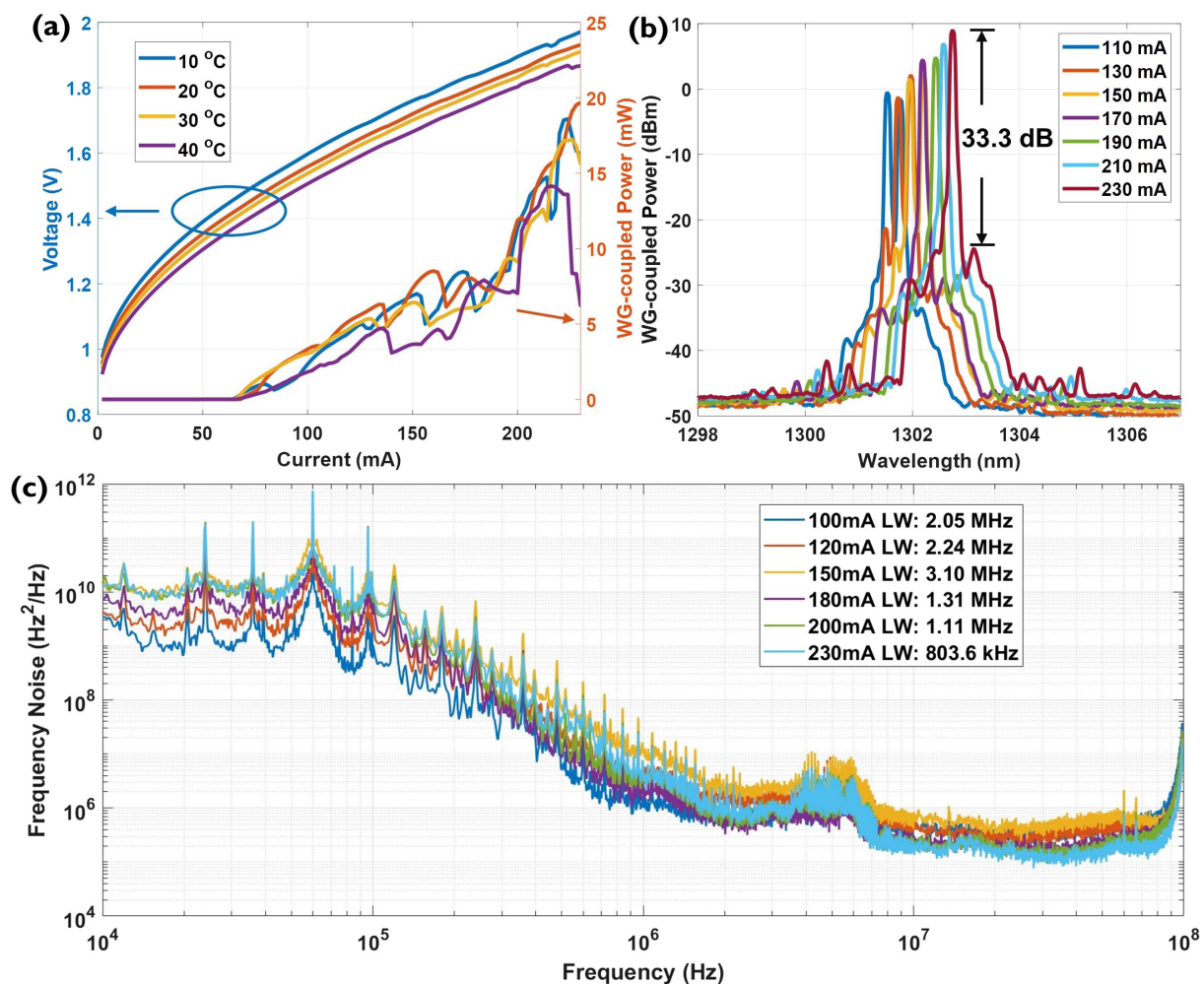


**Fig. 6.** (a) Current-voltage (*IV*) characteristics and WG-coupled output power of the GaAs QD-on-Si DFB laser at various temperatures; (b) optical spectra of the GaAs QD-on-Si DFB laser at different drive currents; (c) frequency noise spectrum of the GaAs QD-on-Si DFB laser at various drive currents, indicating linewidth values from 2.05 MHz to 803.6 kHz.

the primary lasing mode stabilizes, achieving a side-mode suppression ratio (SMSR) of up to 33 dB.

Figure 6(c) shows the frequency noise spectrum and instantaneous linewidth (LW) of the DFB lasers, which is acquired by an OE4000 laser phase noise analyzer system. It shows that when the bias current increases, the linewidth of the device decreases from 2.05 MHz to 803.6 kHz, because a higher proportion of stimulated emission results in reduced phase noise, as the phase of the emitted photons becomes more synchronized with the optical field inside the cavity [55]. This reduced phase noise narrows the spectral linewidth of the laser.

Furthermore, in the operation of DFB lasers, the recombination and generation of carriers and photons result in instantaneous fluctuations in photon density. These fluctuations lead to variations in the output power, known as the relative intensity noise (RIN) of the laser [56–58]. High RIN levels can increase the bit error rate (BER) in optical communication systems by causing random variations in signal amplitude, potentially leading to incorrect data interpretation at the receiver end [59–61]. Therefore, for high-speed applications, it is crucial to use DFB lasers with low RIN. In designing a communication system, the desired BER sets an upper limit on the allowable RIN of the laser. The RIN per unit bandwidth can be calculated using the formula [62]

$$\text{RIN(dB/Hz)} = 10 \log_{10} \left( \frac{\langle (\delta P(t))^2 \rangle}{P_0^2} \right) - 10 \log_{10}(\Delta f), \tag{1}$$

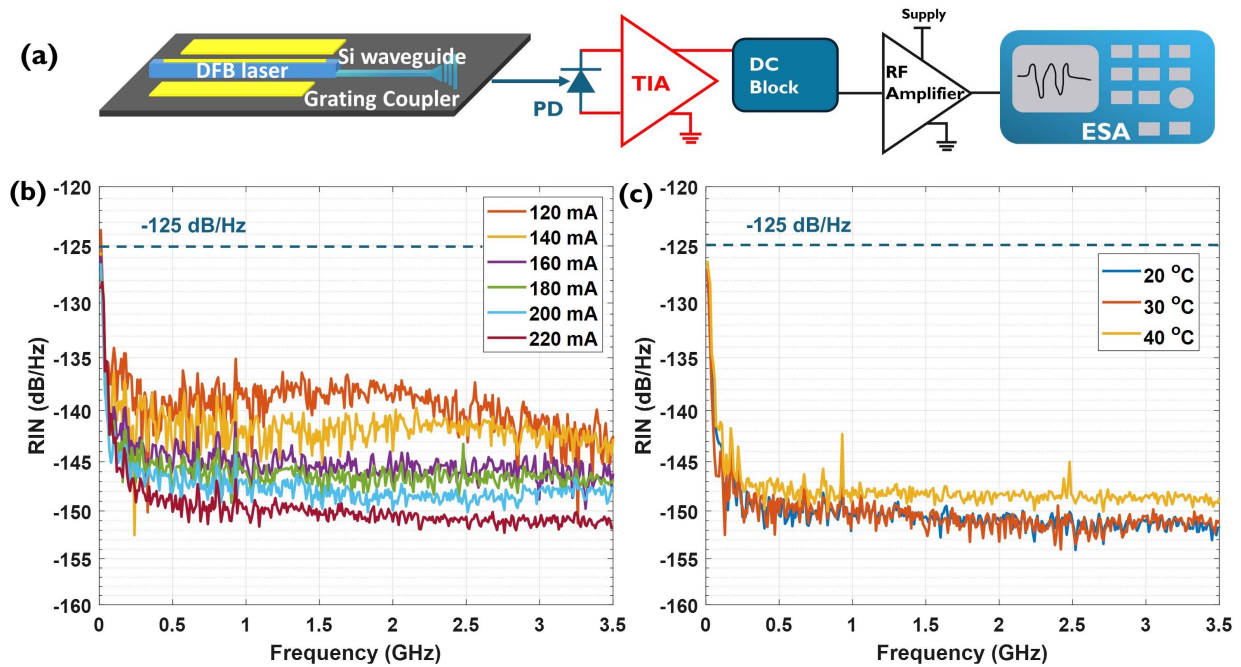
where  $\langle (\delta P(t))^2 \rangle$  represents the mean-square noise fluctuation (assumed to follow a Gaussian distribution),  $P_0$  denotes the average optical power output of the laser, and  $\Delta f$  is the filter bandwidth of the measurement apparatus. For a digital link operating at 30 Gbps with a required BER of  $10^{-9}$ , assuming

that the required bandwidth is 0.75 of the link bit rate [63], the RIN should be lower than  $-125.0$  dB/Hz. This ensures reliable data transmission with minimal signal degradation.

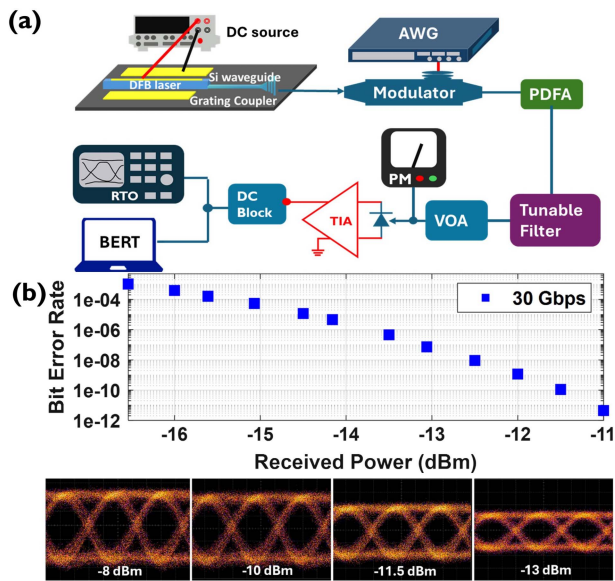
To evaluate the RIN of the QD-on-Si DFB lasers, a measurement setup was constructed as shown in Fig. 7(a). The lasers were driven at various currents, and the emitted light was coupled into an optical fiber. The optical signal was then converted to an electrical signal using a high-speed photodetector (PD) with a transimpedance amplifier (TIA) (Discovery DSCR409). This electrical signal was subsequently passed through a DC block to filter out the DC component, allowing only the RF signal to pass. The RF signal was amplified using an RF amplifier (SHF S804B) before being analyzed by an electrical spectrum analyzer (ESA, Keysight N9010A) to determine the RIN of the laser. It is important to note that the measured noise includes contributions from the laser's RIN, the shot noise of the PD, and the thermal noise of the RF amplifier and TIA. Therefore, a calibration process was conducted to isolate the laser's RIN from these other noise sources.

Figure 7(b) shows the RIN results of the laser under different drive currents. The data indicate that the RIN decreases from  $-137.9$  to  $-149.6$  dB/Hz as the drive current increases from 120 to 220 mA at  $20^\circ\text{C}$ . This reduction in RIN with increasing current can be explained by a decrease in relative photon number fluctuations due to spontaneous emission, which becomes smaller relative to the total photon number at higher currents. Additionally, mode competition is reduced, minimizing power fluctuations between different modes, thereby lowering the RIN.

Figure 7(c) presents the RIN results at temperatures ranging from  $20^\circ\text{C}$  to  $40^\circ\text{C}$  with a fixed drive current of 220 mA. A slight increase in RIN from  $-149.6$  to  $-147.6$  dB/Hz is observed, indicating that noise fluctuations in the laser output increase when operating in a higher-temperature environment.



**Fig. 7.** (a) Schematic diagram of the setup used for measuring the RIN of the QD-on-Si DFB lasers; (b) measured RIN spectra of the DFB laser at a constant temperature of  $20^\circ\text{C}$  under varying drive currents; (c) measured RIN spectra at a fixed drive current of 220 mA at different temperatures.



**Fig. 8.** (a) Schematic diagram of the experimental setup used for high-speed transmission testing of the GaAs QD-on-Si DFB laser; (b) bit error rate as a function of received optical power at a 30 Gbps rate; the inset shows eye diagrams corresponding to different received powers.

Despite this, the laser maintains a relatively low RIN, which is essential for high-speed communication applications.

To further validate the suitability of the GaAs QD-on-Si lasers for high-speed communication applications, we conducted a high-speed transmission test using the setup depicted in Fig. 8(a). In this setup, the laser emission from the on-chip grating coupler is transmitted to an optical modulator, driven by an arbitrary waveform generator (AWG, Agilent Keysight) acting as the signal source, using a pseudo random binary sequence (PRBS) pattern of  $2^7 - 1$  with a non-return-to-zero (NRZ) coding scheme. The modulated optical signal then passes through a PDFA, a tunable optical filter, and a variable optical attenuator (VOA) to control the signal power. The resulting optical signal is converted into an electrical signal by a high-speed PD with TIA (Discovery DSCR409) and is subsequently analyzed using a real time oscilloscope (RTO, LabMaster 10-Zi-A) to capture the eye diagram. The signal is also sent to an SHF bit error rate tester (BERT) to calculate the bit error rate (BER). As illustrated in Fig. 8(b), the DFB laser demonstrates robust performance, supporting a 30 Gbps digital link with high fidelity. When the received power at the photodetector exceeds  $-11$  dBm, the BER is lower than  $10^{-12}$ , which is below the threshold of the BERT, indicating excellent signal integrity.

### C. Performance of Integrated GaAs QD-on-Si Widely Tunable Lasers

The performance of the O-band QD-on-Si widely tunable lasers was evaluated on a temperature-controlled stage. To ensure stable and reliable electrical connections during testing, the devices were wire-bonded onto a printed circuit board (PCB). This setup, implemented using the PyMeasure3 library, efficiently controlled the SourceMeter for thermal tuning while monitoring the output with an HP power meter and OSA,

enhancing measurement accuracy and repeatability. The lasers exhibited a threshold current of 80 mA, as shown in the *LIV* characteristics in Fig. 9(a). The differential resistance was less than  $3 \Omega$ . The WG output power at 1295.8 nm reaches 3.6 mW at  $20^\circ\text{C}$ .

The tuning mechanism of the laser was based on the Vernier filter, which utilized two thermally tunable micro-ring resonators with slightly different diameters to achieve wide tunability. Additionally, a thermally tunable Sagnac loop mirror and a phase shifter were employed to optimize the reflectivity of the out-coupling mirror and enhance the tuning accuracy and output power. The tuning principle can be referenced from the cited literature [64]. The wavelength tuning range spanned from 1280.6 to 1315.7 nm, over 35 nm, as shown in Fig. 9(b). The lasers maintained a high SMSR of approximately 40 dB across the entire tuning range, ensuring stable single-mode operation with minimal mode competition.

The results confirm the potential of these GaAs QD-on-Si widely tunable lasers on SiPh systems, offering broad wavelength tunability, good output power, and spectral purity, making them interesting for integration into advanced SiPh platforms. These capabilities pave the way for future innovations in high-capacity optical communication systems and other applications requiring compact, efficient, and highly tunable photonic devices.

### D. Dynamic Response of DFB Lasers under Optical Feedback

In communication systems, light emitted from the laser passes through various optical components, leading to some degree of reflection at each interface inevitably. These reflections can adversely affect the performance of the laser [65–67]. When the level of external optical feedback reaches a certain threshold, it can cause a phenomenon known as coherence collapse [68–70]. Even minimal amounts of feedback can have substantial effects on the laser's linewidth and noise characteristics, particularly for single-frequency quantum well based lasers. In fact, feedback as low as 0.4% ( $-24$  dB) is considered significant [62]. In fiber-optic communication systems, isolators are typically placed in front of the laser to prevent external light feedback from degrading the laser's optical quality [71]. For on-chip SiPh systems, recent research has explored the use of magneto-optic non-reciprocal materials such as Ce:YIG or bismuth-substituted YIG (Bi:YIG) to fabricate isolators that can prevent reflections within the photonic integrated circuit (PIC) from re-entering the laser cavity and affecting its performance [72–75]. However, integrating such isolators into the PIC requires complex circuit design, which adds additional fabrication steps and increases the overall cost of the device.

To achieve high-quality on-chip laser sources, we selected quantum dots as the active layers for our GaAs active devices. Previous research has shown that QD active layers exhibit lower sensitivity to optical feedback compared to quantum wells [76,77]. This is primarily because QD active layers typically have a low linewidth enhancement factor ( $\alpha_H$ ), which quantifies the coupling between phase noise and intensity noise in a laser, and a high damping rate. A small  $\alpha_H$  indicates weak coupling between changes in gain and changes in refractive index. Consequently, when a laser with a low  $\alpha_H$  is

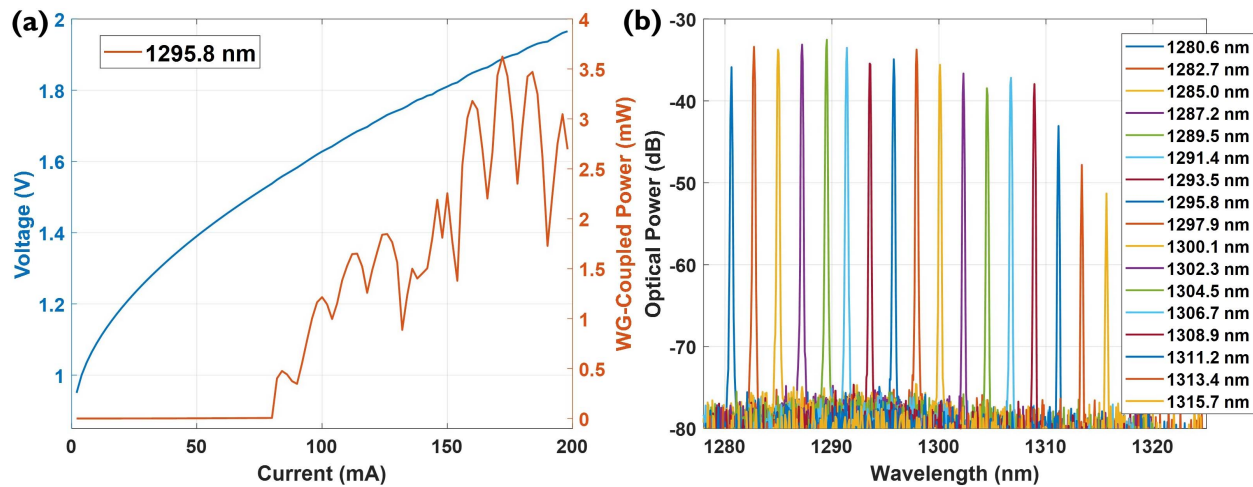


**Fig. 9.** (a) *IV* characteristics and WG-coupled output power of the GaAs QD-on-Si widely tunable laser with the resonant wavelength tuned to 1295.8 nm; (b) optical spectrum of the tunable laser.

disturbed by an optical feedback signal, the resulting changes in gain and phase are less likely to influence each other, leading to a more stable laser output and reduced sensitivity to feedback.

Additionally, in QD lasers, off-resonance energy states significantly affect laser dynamics. QD lasers can operate in three different lasing regimes depending on the bias conditions: (i) ground state (GS) lasing, (ii) first excited state (ES) lasing, and (iii) dual-state lasing where both GS and ES are active [78]. Research on GaAs QD lasers has shown that those devices lasing exclusively from the GS transition are much more stable under external optical feedback than those operating in dual-state or ES-only lasing regimes [77,79]. Recent studies have further demonstrated that for GaAs QD lasers that can switch between the GS and ES lasing, the level of feedback that causes instability depends a lot on the threshold difference between ES and GS [78]. If the laser switches quickly from GS to ES, it is more likely to become unstable when they are under optical feedback.

To evaluate the GaAs QD-on-Si DFB laser's sensitivity to external optical feedback and verify its robustness for high-speed on-chip optical communication, we designed a measurement setup to examine the impact of optical feedback on the RIN of the DFB lasers. The experimental setup, illustrated in Fig. 10, involves directing the emission from the GaAs QD-on-Si DFB laser through a grating coupler structure, after which the output is split into two paths using a 3 dB splitter. In the first path, the laser signal is routed into an optical circulator, with the output port (port 3) connected back to the input port (port 1) to create a feedback loop. Between ports 1 and 3, a variable optical attenuator (VOA) and an SOA with a tunable filter are introduced to precisely control the optical feedback level into the DFB laser. When the feedback level exceeds  $-25$  dB, the SOA amplifies the laser signal within the loop to increase the feedback strength directed back into the laser. The second path directs the laser output to the RIN measurement system, as shown in Fig. 7(a), to assess how varying levels of optical feedback affect the noise characteristics of the DFB laser.

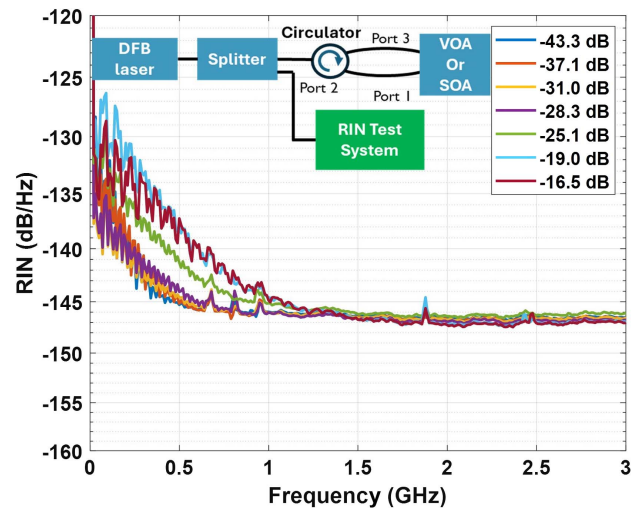


**Fig. 10.** Measured RIN spectra of the DFB lasers with different feedback levels into the lasers driven at 230 mA (the inset is the setup for measuring the laser RIN with optical feedback).

Figure 10 presents the RIN results of the QD-on-Si DFB lasers under varying levels of optical feedback, with the DFB laser operating at a drive current of 230 mA. The data indicate that at high frequencies ( $>1$  GHz), the RIN of the laser remains relatively unaffected by changes in feedback level, with the RIN values remaining nearly constant. This is because at the high-frequency region of the RIN spectrum, quantum noise (primarily shot noise due to spontaneous emission) is the dominant noise source [62]. The noise is typically white noise, which shows insensitivity to optical feedback. However, at lower frequencies, a noticeable difference in RIN is observed, due to the interaction with relaxation oscillations. The laser becomes more sensitive to external optical feedback at these lower frequencies, which can induce fluctuations in the optical power and thereby increase the RIN. Notably, even with a strong external optical feedback level, such as  $-16.5$  dB, the RIN peak at

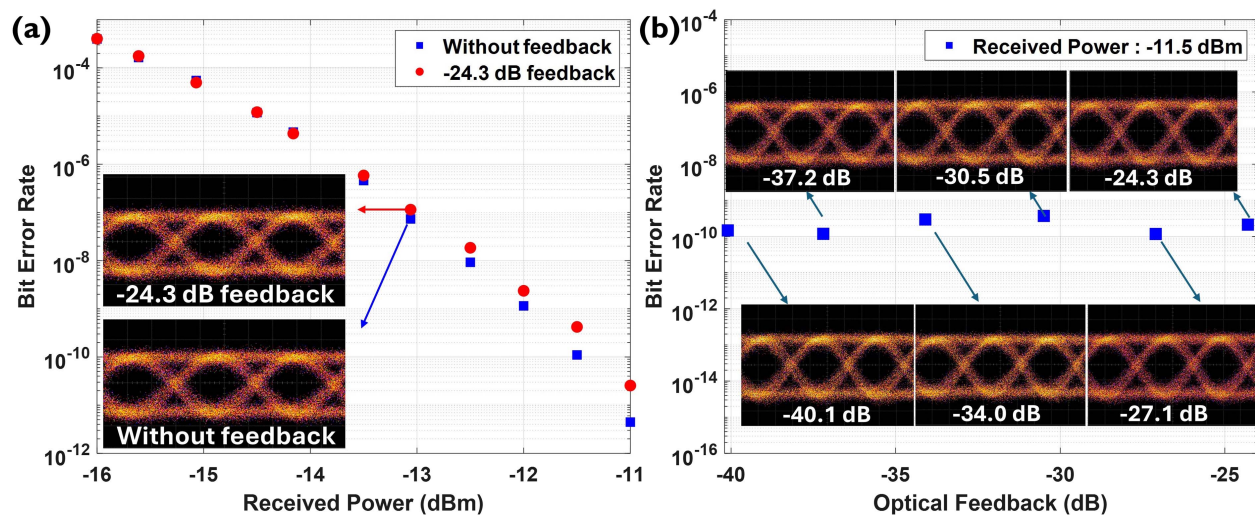


**Fig. 11.** (a) BER versus the received power with and without optical feedback; (b) BER versus different optical feedback levels; the inset shows eye diagrams corresponding to varying feedback levels.

low frequencies remains below  $-125.0$  dB/Hz. This value is critical, as it is sufficient to support a 30 Gbps optical communication link, as discussed in the previous section.

To further validate the QD-on-Si DFB laser's robustness against optical feedback, we integrated the optical feedback path into the 30 Gbps high-speed transmission test setup. As illustrated in Fig. 11(a), even with the introduction of an optical feedback level as high as  $-24.3$  dB (which is considered reasonably attainable in a well designed optical system), the relationship between BER and received power remains similar, indicating that the high feedback level does not notably affect the GaAs QD-on-Si DFB lasers performance. Specifically, at a received power of  $-11$  dBm, the BER without any feedback is  $4.44 \times 10^{-12}$ , while with a  $-24.3$  dB feedback, the BER slightly increases to  $2.56 \times 10^{-11}$ . Additionally, the eye diagrams with and without optical feedback show no significant degradation; they remain clear and open, demonstrating stable signal quality under high-feedback conditions. Figure 11(b) presents the BER results and the corresponding eye diagrams at various feedback levels, illustrating that the BER remains low and stable, consistently around  $10^{-10}$ .

#### 4. CONCLUSION

In this study, we successfully demonstrated the integration of pre-fabricated standardized InAs/GaAs QD active devices onto a SiPh platform using  $\mu$ TP technology. By strategically placing these QD devices onto designated regions of the SiPh chip, we fabricated O-band optical amplifiers, isolator-free DFB lasers, and widely tunable lasers directly on the chip, enabling efficient signal amplification and laser output. The integrated SOAs achieved a maximum on-chip gain of 7.5 dB, while the DFB lasers delivered waveguide output powers of up to 19.7 mW at room temperature, supporting error-free data transmission at 30 Gbps under external modulation. The widely tunable lasers demonstrated a wavelength tuning range exceeding 35 nm, and a waveguide output power greater than 3 mW. The quantum dot structure of the active layers results in

robustness against external optical feedback, as evidenced by minimal degradation in relative intensity noise and stable bit error rates under high-speed operation. These results highlight the potential of  $\mu$ TP technology for developing fully integrated O-band SiPh chips, providing a viable path towards compact, high-performance photonic circuits capable of supporting high-speed, high-capacity optical communication.

**Funding.** European Union (CALADAN) (825453); Dutch Growth Fund PhotonDelta project.

**Disclosures.** The authors declare no conflicts of interest.

**Data Availability.** Data underlying the results presented in this paper are not publicly available at this time but may be obtained from the authors upon reasonable request.

#### REFERENCES

1. S. Shekhar, W. Bogaerts, L. Chrostowski, *et al.*, "Roadmapping the next generation of silicon photonics," *Nat. Commun.* **15**, 751 (2024).
2. D. Liang, G. Roelkens, R. Baets, *et al.*, "Hybrid integrated platforms for silicon photonics," *Materials* **3**, 1782–1802 (2010).
3. D. Thomson, A. Zilkie, J. E. Bowers, *et al.*, "Roadmap on silicon photonics," *J. Opt.* **18**, 073003 (2016).
4. S. Y. Siew, B. Li, F. Gao, *et al.*, "Review of silicon photonics technology and platform development," *J. Lightwave Technol.* **39**, 4374–4389 (2021).
5. A. Novack, M. Streshinsky, R. Ding, *et al.*, "Progress in silicon platforms for integrated optics," *Nanophotonics* **3**, 205–214 (2014).
6. F. Ferraro, P. De Heyn, M. Kim, *et al.*, "IMEC silicon photonics platforms: performance overview and roadmap," *Proc. SPIE* **12429**, 1242909 (2023).
7. M. de Cea, D. Van Orden, J. Fini, *et al.*, "High-speed, zero-biased silicon-germanium photodetector," *APL Photonics* **6**, 041302 (2021).
8. G. Chen, Y. Yu, Y. Shi, *et al.*, "High-speed photodetectors on silicon photonics platform for optical interconnect," *Laser Photonics Rev.* **16**, 220C0117 (2022).
9. J. Michel, J. Liu, and L. C. Kimerling, "High-performance Ge-on-Si photodetectors," *Nat. Photonics* **4**, 527–534 (2010).

10. C. Galland, A. Novack, Y. Liu, *et al.*, "A CMOS-compatible silicon photonic platform for high-speed integrated opto-electronics," *Proc. SPIE* **8767**, 87670G (2013).
11. A. Rahim, E. Ryckeboer, A. Z. Subramanian, *et al.*, "Expanding the silicon photonics portfolio with silicon nitride photonic integrated circuits," *J. Lightwave Technol.* **35**, 639–649 (2017).
12. S. Cheung, D. Liang, Y. Yuan, *et al.*, "Ultra-power-efficient, electrically programmable, multi-state photonic flash memory on a heterogeneous III-V/Si platform," *Laser Photonics Rev.* **18**, 2400001 (2024).
13. W. Bogaerts and L. Chrostowski, "Silicon photonics circuit design: methods, tools and challenges," *Laser Photonics Rev.* **12**, 1700237 (2018).
14. K. A. Buzaverov, A. S. Baburin, E. V. Sergeev, *et al.*, "Silicon nitride integrated photonics from visible to mid-infrared spectra," *Laser Photonics Rev.* **18**, 2400508 (2024).
15. D. Liang, G. Kurczveil, X. Huang, *et al.*, "Heterogeneous silicon light sources for datacom applications," *Opt. Fiber Technol.* **44**, 43–52 (2018).
16. D. Liang and J. E. Bowers, "Recent progress in lasers on silicon," *Nat. Photonics* **4**, 511–517 (2010).
17. W. L. Ng, M. Lourenco, R. Gwilliam, *et al.*, "An efficient room-temperature silicon-based light-emitting diode," *Nature* **410**, 192–194 (2001).
18. J. A. Bebawi, I. Kandas, M. A. El-Osairy, *et al.*, "A comprehensive study on EDFA characteristics: temperature impact," *Appl. Sci.* **8**, 1640 (2018).
19. Y. Nishida, M. Yamada, T. Kanamori, *et al.*, "Development of an efficient praseodymium-doped fiber amplifier," *IEEE J. Quantum Electron.* **34**, 1332–1339 (1998).
20. C. Wang, X.-L. Zhong, and Z.-Y. Li, "Linear and passive silicon optical isolator," *Sci. Rep.* **2**, 674 (2012).
21. P. Pintus, F. Di Pasquale, and J. E. Bowers, "Integrated TE and TM optical circulators on ultra-low-loss silicon nitride platform," *Opt. Express* **21**, 5041–5052 (2013).
22. W. Yan, Z. Wei, Y. Yang, *et al.*, "Ultra-broadband magneto-optical isolators and circulators on a silicon nitride photonics platform," *Optica* **11**, 376–384 (2024).
23. M. P. Rombouts, F. Karinou, P. Pintus, *et al.*, "A sub-picojoule per bit integrated magneto-optic modulator on silicon: modeling and experimental demonstration," *Laser Photonics Rev.* **17**, 2200799 (2023).
24. J. Zhang, M. A. Itzler, H. Zbinden, *et al.*, "Advances in InGaAs/InP single-photon detector systems for quantum communication," *Light Sci. Appl.* **4**, e286 (2015).
25. D. Saxena, S. Mokkapatil, P. Parkinson, *et al.*, "Optically pumped room-temperature GaAs nanowire lasers," *Nat. Photonics* **7**, 963–968 (2013).
26. S.-I. Nagahama, T. Yanamoto, M. Sano, *et al.*, "Ultraviolet GaN single quantum well laser diodes," *Japan J. Appl. Phys.* **40**, L785 (2001).
27. Y. Zheng, C. Sun, B. Xiong, *et al.*, "Integrated gallium nitride nonlinear photonics," *Laser Photonics Rev.* **16**, 2100071 (2022).
28. D. Liang, S. Srinivasan, A. Descos, *et al.*, "High-performance quantum-dot distributed feedback laser on silicon for high-speed modulations," *Optica* **8**, 591–593 (2021).
29. Y. Qi and Y. Li, "Integrated lithium niobate photonics," *Nanophotonics* **9**, 1287–1320 (2020).
30. X. Liu, N. Chen, and T. Chu, "Polarization-insensitive electrooptic modulation on anisotropic thin-film lithium niobate," *ACS Photonics* **11**, 2556–2560 (2024).
31. D. Ban, G. Liu, H. Yu, *et al.*, "High electro-optic coefficient lead zirconate titanate films toward low-power and compact modulators," *Opt. Mater. Express* **11**, 1733–1741 (2021).
32. C. Wang, Z. Li, J. Riemensberger, *et al.*, "Lithium tantalate photonic integrated circuits for volume manufacturing," *Nature* **629**, 784–790 (2024).
33. Z. Wei, W. Yan, J. Qin, *et al.*, "Dysprosium substituted Ce:YIG thin films for temperature insensitive integrated optical isolator applications," *Materials* **15**, 1691 (2022).
34. S. Ghosh, S. Keyavania, W. Van Roy, *et al.*, "Ce:YIG/silicon-on-insulator waveguide optical isolator realized by adhesive bonding," *Opt. Express* **20**, 1839–1848 (2012).
35. J. Liang, Y. Li, T. Dai, *et al.*, "On-chip Ce:YIG/Si Mach-Zehnder optical isolator with low power consumption," *Opt. Express* **31**, 8375–8383 (2023).
36. G. Roelkens, J. Zhang, L. Bogaert, *et al.*, "Present and future of micro-transfer printing for heterogeneous photonic integrated circuits," *APL Photonics* **9**, 010901 (2024).
37. Y. Liu, L. Wang, Y. Zhang, *et al.*, "Demonstration of n-Ga<sub>2</sub>O<sub>3</sub>/p-GaN diodes by wet-etching lift-off and transfer-print technique," *IEEE Electron. Device Lett.* **42**, 509–512 (2021).
38. J. Justice, C. Bower, M. Meitl, *et al.*, "Wafer-scale integration of group III-V lasers on silicon using transfer printing of epitaxial layers," *Nat. Photonics* **6**, 610–614 (2012).
39. Y. Liu, Z. Li, F. B. Atar, *et al.*, "Integration of high-performance InGaAs/GaN photodetectors by direct bonding via micro-transfer printing," *ACS Appl. Mater. Interfaces* **16**, 10996–11002 (2024).
40. S. Uvin, S. Kumari, A. De Groote, *et al.*, "1.3 μm InAs/GaAs quantum dot DFB laser integrated on a Si waveguide circuit by means of adhesive die-to-wafer bonding," *Opt. Express* **26**, 18302–18309 (2018).
41. S. Dhoore, S. Uvin, D. Van Thourhout, *et al.*, "Novel adiabatic tapered couplers for active III-V/SOI devices fabricated through transfer printing," *Opt. Express* **24**, 12976–12990 (2016).
42. N. Ye, G. Muliuk, J. Zhang, *et al.*, "Transfer print integration of waveguide-coupled germanium photodiodes onto passive silicon photonic ICs," *J. Lightwave Technol.* **36**, 1249–1254 (2018).
43. T. Vanackere, T. Vandekerckhove, L. Bogaert, *et al.*, "Heterogeneous integration of a high-speed lithium niobate modulator on silicon nitride using micro-transfer printing," *APL Photonics* **8**, 086102 (2023).
44. J. R. Vaskasi, N. Singh, J. Van Kerrebrouck, *et al.*, "High wall-plug efficiency and narrow linewidth III-V-on-silicon C-band DFB laser diodes," *Opt. Express* **30**, 27983–27992 (2022).
45. Q. Cai, P. Li, Y. Shi, *et al.*, "Tbps parallel random number generation based on a single quarter-wavelength-shifted DFB laser," *Opt. Laser Technol.* **162**, 109273 (2023).
46. M. A. Tran, D. Huang, and J. E. Bowers, "Tutorial on narrow linewidth tunable semiconductor lasers using Si/III-V heterogeneous integration," *APL Photonics* **4**, 111101 (2019).
47. E. Soltanian, G. Muliuk, S. Uvin, *et al.*, "Micro-transfer-printed narrow-linewidth III-V-on-Si double laser structure with a combined 110 nm tuning range," *Opt. Express* **30**, 39329–39339 (2022).
48. T. Komljenovic, L. Liang, R.-L. Chao, *et al.*, "Widely-tunable ring-resonator semiconductor lasers," *Appl. Sci.* **7**, 732 (2017).
49. C. Yu, Z. Chen, J. J. Wang, *et al.*, "Temperature dependence of the band gap of perovskite semiconductor compound CsSn<sub>3</sub>," *J. Appl. Phys.* **110**, 063526 (2011).
50. J. Camassel, D. Auvergne, and H. Mathieu, "Temperature dependence of the band gap and comparison with the threshold frequency of pure GaAs lasers," *J. Appl. Phys.* **46**, 2683–2689 (1975).
51. D. P. Popescu, P. G. Eliseev, A. Stintz, *et al.*, "Temperature dependence of the photoluminescence emission from InAs quantum dots in a strained Ga<sub>0.85</sub>In<sub>0.15</sub>As quantum well," *Semicond. Sci. Technol.* **19**, 33 (2003).
52. R. Fehse, S. Tomic, A. R. Adams, *et al.*, "A quantitative study of radiative, Auger, and defect related recombination processes in 1.3-μm GaInNAs-based quantum-well lasers," *IEEE J. Sel. Topics Quantum Electron.* **8**, 801–810 (2002).
53. K. Hild, S. J. Sweeney, I. P. Marko, *et al.*, "Temperature and pressure dependence of carrier recombination processes in GaAsSb/GaAs quantum well lasers," *Phys. Status Solidi* **244**, 197–202 (2007).
54. E. Kioupakis, Q. Yan, D. Steiauf, *et al.*, "Temperature and carrier-density dependence of auger and radiative recombination in nitride optoelectronic devices," *New J. Phys.* **15**, 125006 (2013).
55. P. Goldberg, P. W. Milonni, and B. Sundaram, "Theory of the fundamental laser linewidth," *Phys. Rev. A* **44**, 1969–1985 (1991).
56. W. Jin, Q.-F. Yang, L. Chang, *et al.*, "Hertz-linewidth semiconductor lasers using CMOS-ready ultra-high-Q microresonators," *Nat. Photonics* **15**, 346–353 (2021).
57. W. Pan, L. Zhang, H. Jiang, *et al.*, "Ultrafast Raman fiber laser with random distributed feedback," *Laser Photonics Rev.* **12**, 1700326 (2018).

58. N. Volet, X. Yi, Q.-F. Yang, *et al.*, "Micro-resonator soliton generated directly with a diode laser," *Laser Photonics Rev.* **12**, 1700307 (2018).
59. D. Yin, A. Gubenko, I. Krestnikov, *et al.*, "Laser diode comb spectrum amplification preserving low RIN for WDM applications," in *2009 Asia Communications and Photonics Conference and Exhibition (ACP)* (IEEE, 2009), pp. 1–7.
60. X. Lu, C. Su, and R. Lauer, "Increase in laser RIN due to asymmetric nonlinear gain, fiber dispersion, and modulation," *IEEE Photonics Technol. Lett.* **4**, 774–777 (1992).
61. A. Akrouf, A. Shen, R. Brenot, *et al.*, "Separate error-free transmission of eight channels at 10 Gb/s using comb generation in a quantum-dash-based mode-locked laser," *IEEE Photonics Technol. Lett.* **21**, 1746–1748 (2009).
62. L. A. Coldren, S. W. Corzine, and M. L. Mashanovitch, *Diode Lasers and Photonic Integrated Circuits*, Vol. **218** (John Wiley & Sons, 2012).
63. G. J. Pendock and D. D. Sampson, "Transmission performance of high bit rate spectrum-sliced WDM systems," *J. Lightwave Technol.* **14**, 2141–2148 (1996).
64. B. Pan, J. Bourderionnet, V. Billault, *et al.*, "III-V-on-Si<sub>3</sub>N<sub>4</sub> widely tunable narrow-linewidth laser based on micro-transfer printing," *Photonics Res.* **12**, 2508–2520 (2024).
65. K.-P. Ho, J. D. Walker, and J. M. Kahn, "External optical feedback effects on intensity noise of vertical-cavity surface-emitting lasers," *IEEE Photonics Technol. Lett.* **5**, 892–895 (1993).
66. A. Locquet, "Routes to chaos of a semiconductor laser subjected to external optical feedback: a review," *Photonics* **7**, 22 (2020).
67. G. Morthier, "Feedback sensitivity of distributed-feedback laser diodes in terms of longitudinal field integrals," *IEEE J. Quantum Electron.* **38**, 1395–1397 (2002).
68. D. Lenstra, B. Verbeek, and A. Den Boef, "Coherence collapse in single-mode semiconductor lasers due to optical feedback," *IEEE J. Quantum Electron.* **21**, 674–679 (1985).
69. F. Grillot, B. Thedrez, O. Gauthier-Lafaye, *et al.*, "Coherence-collapse threshold of 1.3- $\mu$ m semiconductor DFB lasers," *IEEE Photonics Technol. Lett.* **15**, 9–11 (2003).
70. S. Azouigui, B. Kelleher, S. Hegarty, *et al.*, "Coherence collapse and low-frequency fluctuations in quantum-dash based lasers emitting at 1.57  $\mu$ m," *Opt. Express* **15**, 14155–14162 (2007).
71. K. Kobayashi and M. Seki, "Microoptic grating multiplexers and optical isolators for fiber-optic communications," *IEEE J. Quantum Electron.* **16**, 11–22 (1980).
72. S. Ghosh, S. Keyvaninia, W. Van Roy, *et al.*, "Adhesively bonded Ce: YIG/SOI integrated optical circulator," *Opt. Lett.* **38**, 965–967 (2013).
73. Y. Shoji and T. Mizumoto, "Magneto-optical non-reciprocal devices in silicon photonics," *Sci. Technol. Adv. Mater.* **15**, 014602 (2014).
74. K. Srinivasan and B. J. Stadler, "Review of integrated magneto-optical isolators with rare-earth iron garnets for polarization diverse and magnet-free isolation in silicon photonics," *Opt. Mater. Express* **12**, 697–716 (2022).
75. L. Bi, J. Hu, P. Jiang, *et al.*, "Magneto-optical thin films for on-chip monolithic integration of non-reciprocal photonic devices," *Materials* **6**, 5094–5117 (2013).
76. G. Morthier, "Numerical study of the single mode stability of quantum well and quantum dot DFB laser diodes under external optical feedback," *IEEE Photonics J.* **15**, 1501204 (2023).
77. J. Duan, H. Huang, B. Dong, *et al.*, "1.3- $\mu$ m reflection insensitive InAs/GaAs quantum dot lasers directly grown on silicon," *IEEE Photonics Technol. Lett.* **31**, 345–348 (2019).
78. H. Huang, J. Duan, D. Jung, *et al.*, "Analysis of the optical feedback dynamics in InAs/GaAs quantum dot lasers directly grown on silicon," *J. Opt. Soc. Am. B* **35**, 2780–2787 (2018).
79. L.-C. Lin, C.-Y. Chen, H. Huang, *et al.*, "Comparison of optical feedback dynamics of InAs/GaAs quantum-dot lasers emitting solely on ground or excited states," *Opt. Lett.* **43**, 210–213 (2018).